

G-MEMP: Gaze-Enhanced Multimodal Ego-Motion Prediction in Driving

M. Eren Akbiyik¹
Christian Vater¹

Nedko Savov²
Otmar Hilliges¹

Danda Pani Paudel^{1,2}
Luc Van Gool^{1,2}

Nikola Popovic¹
Xi Wang¹

¹ETH Zürich ²INSAIT, Sofia University

Abstract

Understanding the decision-making process of drivers is one of the keys to ensuring road safety. While the driver intent and the resulting ego-motion trajectory is valuable in developing driver-assistance systems, existing methods mostly focus on the motions of other vehicles. In contrast, we focus on inferring the ego-trajectory of a driver’s vehicle using their gaze data. For this purpose, we first collect a new dataset, GEM, which contains high-fidelity ego-motion videos paired with drivers’ eye-tracking data and GPS coordinates. Next, we develop G-MEMP, a novel multimodal ego-trajectory prediction network that combines GPS and video input with gaze data. We also propose a new metric called Path Complexity Index (PCI) to measure the trajectory complexity. We perform extensive evaluations of the proposed method on both GEM and DR(eye)VE, an existing benchmark dataset. The results show that G-MEMP significantly outperforms state-of-the-art methods in both benchmarks. Furthermore, ablation studies demonstrate over 20% improvement in average displacement using gaze data, particularly in challenging driving scenarios with a high PCI. The data, code, and models can be found at <https://eth-ait.github.io/g-memp/>.

1. Introduction

Understanding the perception and decision-making process of drivers is crucial for road safety in autonomous and assisted driving. Statistics reveal that 42% of car-bicycle collisions result from driver inattention [1]. In response, a driver-assistance system capable of refining human input based on the predicted intent of the driver would enable vehicles to make informed decisions [38]. While understanding drivers’ intent is critical for inferring their future trajectories, traditional methods mostly focus on predicting the paths of other vehicles [13, 25, 26, 36, 46]. In contrast, we seek to predict drivers’ ego-trajectory and to infer their intent with the help of gaze input.

This setting presents a dynamic interplay of imminent and long-term intent, influenced by the surrounding traffic.

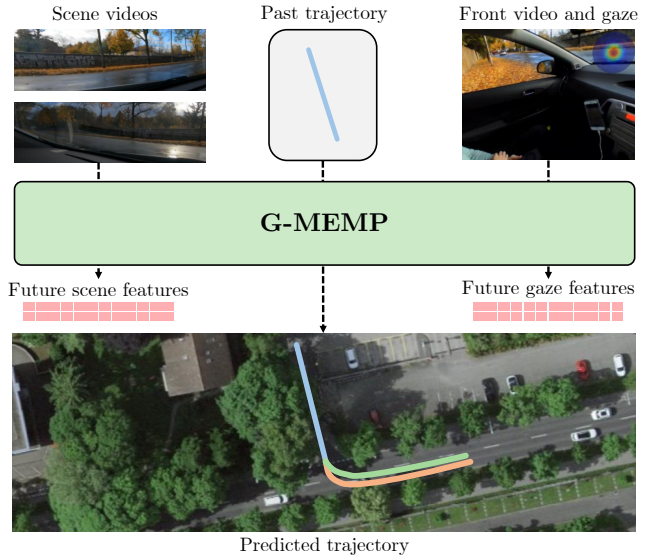


Figure 1. **G-MEMP framework.** Using the scene videos, gaze, and past GPS coordinates, we predict the future trajectory (in comparison to the target trajectory). The training is regularized through predicted scene and gaze features.

Our central idea builds on the insight that the gaze of a person is tightly intertwined with their intent in varying horizons [3, 15, 53]. Especially in driving, the direction and focus of a driver’s gaze can reveal important information about their decisions on the road. For instance, a driver whose gaze fixates on the brake lights of the vehicle ahead is likely to decelerate promptly, reflecting an imminent intent to slow down, as seen in Figure 2. While regular driving scenarios range from steady cruising to navigating intersections, the greatest value of being able to predict ego-trajectories emerge in ambiguous, complex road paths, e.g., cases where the road is not trivially straight or when predicting where the driver would turn at an intersection. Our focus is thus twofold: firstly, to develop an efficient method for detecting these rare yet valuable scenarios in existing data, and secondly, to establish a framework capable of understanding the driver’s intent in such complex situations for ego-trajectory prediction. To this end, we present a new dataset, a novel metric, and an end-to-end framework.

We first introduce a *Gaze-assisted Ego Motion* (GEM) dataset that captures diverse urban driving scenarios across 10 subjects, integrating GPS, eye gaze, and high-resolution scene data from three cameras—two frontal dash cameras and one positioned on the driver’s glasses (see Figure 1). To bolster accuracy, GPS data has been manually corrected, ensuring precise capture of vehicular speed and acceleration dynamics. To better quantify the task complexity, we propose a new metric named *Path Complexity Index* (PCI), which measures the divergence of a driving trajectory from an anticipated path. It allows us to link trajectory complexity with model performance. Finally, we build a multimodal framework, G-MEMP (Gaze-Enhanced Multimodal Ego-Motion Prediction), for egocentric trajectory estimation that integrates scene data, gaze patterns, and past trajectory (see Figure 1). We train G-MEMP with auxiliary tasks of predicting future gaze and scene features for regularization, using a novel future-discounted loss formulation. Both qualitative and quantitative experimental results show that G-MEMP outperforms state-of-the-art (SOTA) methods on the GEM dataset. To test the generalization ability, we also evaluate G-MEMP on the DR(eye)VE dataset [31], and our method surpasses the SOTA approaches. Ablation studies show that incorporating the gaze information improves the prediction quality, and our proposed model particularly excels in high-PCI situations.

In summary, our contributions are:

- GEM, a dataset with high-fidelity ego-motion videos coupled with accurate GPS coordinates and gaze data.
- PCI, a metric that measures the trajectory complexity.
- G-MEMP, a multimodal ego-motion prediction network that effectively utilizes gaze data with a novel loss design.
- Experiments show that G-MEMP significantly outperforms SOTA approaches on all metrics and gaze data helps especially in high-PCI situations, with over 20% improvement in average displacement for 70+ PCI.

2. Related Work

Eye gaze and intent. Individuals tend to focus on relevant objects in situations with a particular goal in view, acquiring necessary information even before they are needed [45, 53]. This effect has been observed for navigation tasks [15] and social contexts [3]. The advancement of autonomous driving and driver-assistance systems highlights the importance of predicting human intent to improve the decision-making of the vehicle’s safety system [17, 38]. This is especially true for adjusting the ego-vehicle’s trajectory when anticipating and responding to potentially dangerous maneuvers.

Trajectory prediction. Predicting the future sequence of locations of a moving entity has been explored for humans [23, 32, 35, 40], road agents [14, 16] and aircraft [52]. Autonomous driving has largely focused on estimating the trajectories of the many agents surrounding the ego-vehicle

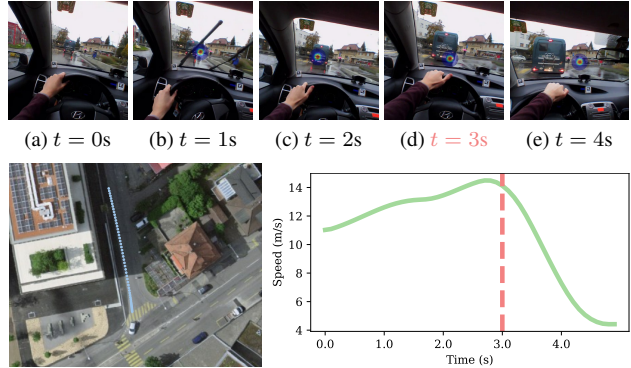


Figure 2. **A sample from the GEM dataset.** The top row shows frames with gaze heatmap overlay on top, at 1 Hz. The bottom left image displays the trajectory of the vehicle, while the bottom right plot shows the speed changes. This is an example of gaze-indicated short-term intent: the driver decelerates as soon as their gaze meets with the brake lights of the vehicle in front.

[13, 25, 26, 36, 46]. However, predicting the ego-vehicles’ trajectory, which is crucial for driving assistance systems, remains less explored. Kinetic models assuming constant velocity and turn rate have been utilized [2]. Kim et al. [19] predict the ego-vehicle’s trajectory with a VAE by conditioning on predicted driving style, while Baumann et al. [4] use observations of the static environment, albeit neither with visual information, similarly with Kim et al. [18] and Feng et al. [8]. Only Malla et al. [24] proposes a vision module but requires hand-annotated actions. Taking a different direction, we focus on leveraging drivers’ intent through gaze behavior observation.

In their work, Jain et al. [17] anticipate vehicle maneuvers using driver behavior footage alongside scene video, while we focus on trajectory prediction using gaze for intent. Yan et al. [50] use head motion and headset gaze for trajectory forecasting by fitting a polynomial, but their low-quality gaze data limits its effectiveness. GIMO [54] introduces a dataset of indoor human motion with gaze data, proving the effectiveness of gaze in enhancing motion trajectory prediction. Inspired by this, our model utilizes gaze data for improved driving ego-trajectory forecasting.

Driving datasets with gaze. In the context of driving, there are datasets that provide in-vehicle footage of the driver’s behavior as an indication of driver’s attention [30], gaze categorized into zones [10, 34] (in a stationary vehicle), head pose [39]. Jain et al. [17] provide both intent-indicative driver video footage and synchronized footage of the scene around the vehicle. However, no gaze data is available. Palazzi et al. [31] provide a dataset of driving under various conditions, with gaze data from a tracking headset and synchronized GPS locations. Given the limited amount of driving datasets with gaze, we introduce a new high-resolution dataset, where accurate eye tracker gaze location and vehicle GPS information are available.

Dataset	Gaze	Noise-free pose/GPS	Scene video quality/rate	Scene cameras	Gaze sampling rate	Duration
Waymo [7]	✗	✓(< 10 cm)	-/10Hz	5	-	574h
nuScenes [5]	✗	✓(< 20 mm)	1080p/12Hz	6	-	5.5h
Argoverse [48]	✗	✓(partially hand-annotated)	2K/20Hz	7	-	305h
LOKI [11]	✗	✗	2K/30Hz	1	-	2.3h
DR(eye)VE [31]	✓	✗	1080p/25Hz	1 (+1 head-cam)	60Hz	6h
GEM (Ours)	✓	✓(hand-annotated)	4K/30Hz	2 (+1 head-cam)	200Hz	5h

Table 1. Comparison of existing trajectory prediction datasets with ours. Although DR(eye)VE is similar to ours but its overall data quality including the GPS positions is significantly worse. Only public datasets are considered.

3. Gaze-assisted Ego Motion (GEM) Dataset

Drivers’ gaze plays a significant role during driving, providing insights about their decisions on the road. Understanding this role may allow us to build systems to improve vehicular safety. However, most driving datasets to train such systems lack either gaze data, noise-free vehicle trajectory, or sufficient quality scene information, as seen in Table 1.

We, therefore, propose GEM, a multimodal ego-motion with gaze dataset with synchronized multi-cam video footage of the road scene, precise gaze locations from an eye-tracking headset and GPS ego-vehicle locations, manually corrected for further accuracy. A sample of the dataset can be seen in Figure 2. By coupling gaze data with the car’s motion and the driving scene, our dataset provides a rich source of information for ego-trajectory prediction and modeling of drivers’ behavior. The primary objective of our dataset is to enable the development and validation of models that can predict driver intent based on their eye movements and surrounding scenes.

3.1. Hardware Setup

We mount high-resolution cameras on the vehicle to ensure high-quality recordings of the surrounding environment and record drivers’ eye gaze using a head-mounted eye tracker. **Frontal cameras and GPS tracking.** To record the driving scene and car motion, we use two GoPro cameras that provide a 4K resolution and a 30Hz sampling rate. These cameras record the car’s GPS positions in real-time and embed this information into the video streams. However, GPS data can have discrepancies due to various factors like satellite interference or obstructions, which we further correct.

Gaze tracking. We employ the Pupil Invisible glasses¹ from Pupil Labs to track the driver’s gaze. This device captures eye movements at 200Hz using two near-eye infrared cameras and includes a frontal video camera of the scene. The gaze tracker and GoPro cameras are fully synchronized in post-processing using the timestamp metadata.

3.2. Data Collection

10 participants were instructed to drive on a variety of road types with a focus on urban areas, during different times of

¹Tech Specs.

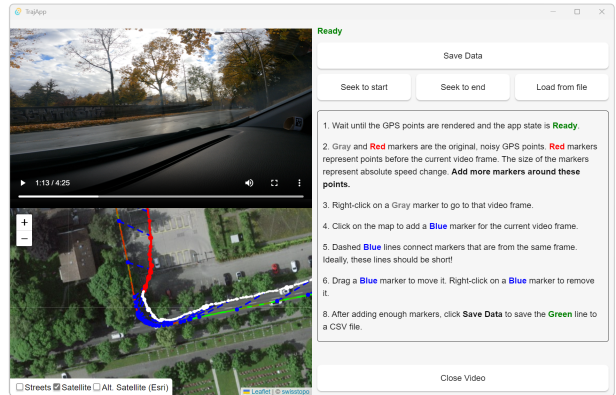


Figure 3. User interface for GPS refinement. We show a video and its corresponding GPS locations on a map concurrently. An annotator places correct markers on the map such that the GPS locations align with the video observations.

the day to capture a comprehensive range of driving conditions. Each participant drove for approximately 30 minutes, resulting in a total of 5 hours of collected data. See Sup. Mat. for a breakdown of the dataset.

Procedure. Upon arrival, participants were briefed about the study and given a tutorial on the equipment. Before commencing the driving sessions, participants went through a gaze calibration process. They were asked to look at specific points on a board, ensuring that the eye-tracking device was accurately capturing their eye movements. After fitting the Pupil Invisible glasses and ensuring proper calibration, participants were asked to start their driving session. A researcher was present in the car to oversee the equipment and address any unexpected situations.

3.3. Post-processing

To enhance the quality of our data, particularly the GPS data, we manually refine the GPS coordinates through a post-processing step. We develop a novel, user-friendly interface and tool that enables annotators to adjust GPS positions projected on a map to synchronize them with the corresponding video input; See the interface in Figure 3. We present the video feed and the noisy GPS locations on a map concurrently, offering a side-by-side comparison. An intuitive interface permits users to correct the GPS markers for the relevant frames of the video. The interface displays the

old markers in gray or red, depending on the currently visible frame of the video, and assigns a larger marker for points with large absolute acceleration. The annotators are asked to place a blue correction marker for all original markers with significant changes in acceleration, such as movements from a still position, and these new markers are interpolated with a piecewise cubic Hermite polynomial [9]. This approach successfully interpolates segments with constant acceleration and does not overshoot if the data is not smooth.

To ensure accurate data annotation, we enlist research assistants trained to use the developed tool. These assistants review the entire dataset, frame by frame, making corrections to the GPS positions wherever necessary. There are checks in place inside the app to ensure the data is fully and densely annotated before the new markers are saved. The annotator can also choose to use different map sources to overlay, including satellite and traffic views. The source code for this tool will be made public together with the dataset, see Sup. Mat. for more details.

We provide a train/validation/test split and detailed content description of the dataset in the Sup. Mat.

4. Path Complexity Index

In autonomous driving, tackling the long tail of driving scenarios — those situations that are less frequent but potentially high-impact — is a critical challenge. These scenarios often encompass a diverse range of unpredictable driving conditions, such as navigating complex intersections or road obstructions. Traditional approaches often view the task as a classification problem, constrained by the limitations of hand-labeling such events [11, 31, 42]. To automatically identify and quantify the complexity of driving situations, we introduce a novel metric termed *Path Complexity Index* (PCI). This metric evaluates the deviation from simple driving patterns, thereby providing a robust tool for assessing and improving trajectory prediction models.

Given an input trajectory, the PCI metric computes the Fréchet distance between the target trajectory and a hypothetical simple trajectory in which the driver maintains the speed and direction exhibited in the last segments of the input trajectory. Formally, the PCI of an observed target trajectory $\mathcal{T}_{target} \in \mathbb{R}^{T \times 2}$ given an input trajectory $\mathcal{T}_{input} \in \mathbb{R}^{T' \times 2}$, is given by:

$$PCI(\mathcal{T}_{target}|\mathcal{T}_{input}) = \inf_{\alpha, \beta \in [0, 1]} \max \left(\sup_{t \in [0, 1]} \|\mathcal{T}_{target}(\alpha(t)) - \mathcal{T}_{simple}(\beta(t))\| \right)$$

where $\alpha : [0, 1] \rightarrow [0, 1]$ and $\beta : [0, 1] \rightarrow [0, 1]$ are continuous non-decreasing functions that represent all reparameterizations of the trajectories [6], and $\mathcal{T}_{simple} \in \mathbb{R}^{T \times 2}$ is the simple trajectory derived by following the final velocity

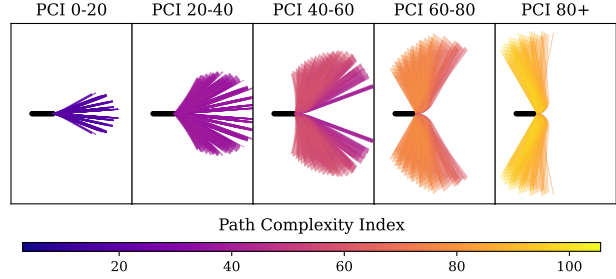


Figure 4. **Generated trajectories and their PCI values.** The black paths to the left of each figure are inputs, and the colored paths are targets generated exhaustively by varying the speed, turning angle, and turn curvature. Notice that as we move to higher PCI, the target paths get longer due to increasing speed.

vector of \mathcal{T}_{input} , defined as:

$$\mathcal{T}_{simple}(t) = \mathcal{T}_{input}(T) + v_{final} \cdot t, \quad t \geq T$$

Here, $v_{final} = \mathcal{T}_{input}(T') - \mathcal{T}_{input}(T' - 1)$ represents the velocity vector estimated from the final two points of \mathcal{T}_{input} , and t is the time parameter extending beyond the duration of the input trajectory T' . $\|\cdot\|$ denotes the Euclidean distance in the 2D plane.

A high value of PCI indicates a significant deviation from the simple trajectory. Some generated examples of deviations from a straight input trajectory and their respective PCI range can be seen in Figure 4. A sample of real trajectories for these ranges are provided in Figure 5. We propose that a high PCI indicates intriguing events, which are often characterized as sudden changes in direction or speed, e.g., turns and stops, in the literature [11]. We provide more insights into this behavior in Sup. Mat. with a comprehensive breakdown of the PCI statistics in GEM dataset.

Are all curved paths interesting? An essential task for trajectory prediction models is learning the road curvature from scene information. PCI is simplistically designed to not bias towards a particular type of curvature to encourage that while allowing us to eliminate instances of straight cruising that may dominate both the training and evaluation phases.

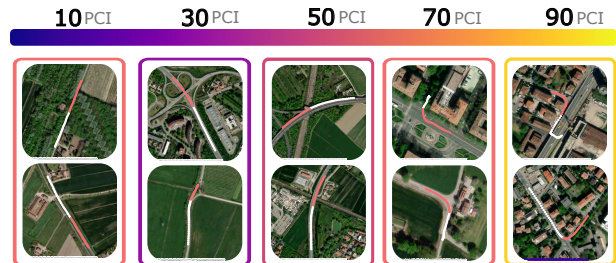


Figure 5. **Example trajectories**, sampled from different ranges of PCI. White is the input and red is the target trajectory.

5. Ego-Motion Prediction with Gaze

Driving is an interplay of short and long-term intent, influenced by exogenous factors. Although such external effects can be understood to some level through computer vision, drivers’ behavior is mostly driven by unobservable intent, which complicates the task of ego-motion prediction. To address this challenge, we propose a new framework named **Gaze-enhanced Multimodal Ego-Motion Prediction (G-MEMP)**. At its core, our method is designed to exploit visual information from multiple cameras, the past trajectory of the vehicle, and, most notably, the driver’s gaze information. Each modality contributes to understanding a different aspect - the surrounding scene, the motion of the vehicle, and the intention of the driver. See [Figure 6](#) for an overview.

G-MEMP offers two key contributions: (1) a novel architecture that fuses multimodal inputs via self- and cross-attention mechanisms for time-series prediction, and (2) various auxiliary losses and future-discounting to regularize long-term forecasting that is otherwise prone to over-fitting.

5.1. Task Definition

In the ego-trajectory prediction task, given measurements of the vehicle and the environment for T time steps, we aim to anticipate the future locations of the vehicle for each of the next T_{pred} time steps (our prediction horizon). For the first T steps, we use as input the vehicle’s motion $M_{1:T}$ and scene representations in the form of video from K cameras of the surroundings $S_{1:T}^{1:K}$. Notably, in addition, we incorporate gaze data $G_{1:T}$. We build a model $\Psi(M_{1:T}, S_{1:T}^{1:K}, G_{1:T}|\lambda) = M_{T+1:T_{\text{pred}}}$ to predict the future motion, where λ are the model’s parameters.

We represent vehicle location with two GPS coordinates using the EPSG:3857 coordinate system (in meters) [12]. The t ’th element of the input motion $M_{1:T} \in \mathbb{R}^{T \times 2}$ corresponds to the relative change of the coordinates compared to $t - 1$, as in Salzmann et al. [37], zero-padded. For each time step $t \in [0, T]$ the scene $S_{1:T}^{1:K} \in \mathbb{R}^{K \times T \times 3 \times H_S^K \times W_S^K}$ contains images from K external vehicle cameras, with width W_S^K and height H_S^K . Gaze data has two components $G_{1:T} = \{G_{1:T}^V; G_{1:T}^L\}$ representing a frontal video feed and the high-frequency gaze positions, respectively. We use frames with width W_G and height H_G from the frontal camera of the eye-tracking headset $G_{1:T}^V \in \mathbb{R}^{T \times 3 \times H_G \times W_G}$. The second component, $G_{1:T}^L \in \mathbb{R}^{T \times 2}$, consists of (x, y) coordinates of points gazed in the image G^V , relative to the bottom-left of the image and normalized in $[0, 1]$.

5.2. G-MEMP Architecture

In our architecture, each of the modalities is processed by a separate encoder $E_M(M_{1:T}) = m_{1:T}$, $E_S(S_{1:T}^{1:K}) = s_{1:T}^{1:K}$ and $E_G(G_{1:T}) = g_{1:T}$, producing sequences of compact

feature vectors with the same size. Next, all K scene features are fused with gaze features using a padded self-attention module $E_P(s_{1:T}^{1:K}, g_{1:T}) = v \in \mathbb{R}^{T \times D}$. Finally, a time-series forecasting module \mathcal{T} predicts the future T_{pred} data points - the future motion, in addition to feature vectors of other modalities, used in training. We design two versions of this architecture: MEMP $\Psi(M_{1:T}, S_{1:T}^{1:K}|\lambda)$, which does not use the gaze features, and G-MEMP $\Psi(M_{1:T}, S_{1:T}^{1:K}, G_{1:T}|\lambda)$, which incorporates all the available modalities, including gaze.

Scene Module. Our shared scene module E_S encodes each frame in $S_{1:T}^{1:K}$ using a pre-trained vision backbone. We experiment with SAM[20], DinoV2[29] and SwinV2[22]. The features are then reduced through 1x1 CNN, pooling, and fully connected layers to produce $s_{1:T} \in \mathbb{R}^{T \times D}$ (see [Figure 6 d2](#)). These features are used in subsequent layers for temporal reasoning with inter-frame attention.

Motion Module. The motion module E_M encodes vehicle motion $M_{1:T}$ through a self-attention mechanism to produce $m_{1:T} \in \mathbb{R}^{T \times D}$ that aligns with the dimensions of other module outputs.

Gaze Module. The frames $G_{1:T}^V$ of the gaze data $G_{1:T}$ are encoded using the same scene encoder E_S , in order to share the representation space and allow for implicit registration between the images. To account for high frame rate of gaze positions and refine the potentially noisy gaze positions, we perform a zero-padded multi-head self-attention of $G_{1:T}^L$, following the decoder design in Zhou et al. [55]. After achieving two encoded feature vectors of the same shape for gaze and frontal video, we perform gaze-frame cross-attention between visual and gaze location features. The attention mechanism allows the model to “pick” the relevant scene features using the gaze positions across frames, thus accounting for the highly dynamic scene in a moving vehicle. The produced vector is $g_{1:T} \in \mathbb{R}^{T \times D}$.

Modality Fusion. The next step is using a fusion module E_P to fuse the obtained motion $m_{1:T}$, scene $s_{1:T}^{1:K}$, and optionally (G-MEMP) gaze $g_{1:T}$ features. To this end, we concatenate $s_{1:T}^{1:K}$ and $g_{1:T}$ across the time dimension, sum with the modality encoding E_D , and push through a self-attention mechanism. E_D encodes the feature source (e.g. encodes the scene ($k \in [0, K]$) and gaze camera identity). This self-attention layer performs implicit image registration and feature selection within and between the scene and gaze modalities. More precisely, we take the concatenation $[s_{1:T}^{1:K}, g_{1:T}] \in \mathbb{R}^{(K+1) \cdot T \times D}$ and produce its fused encoding $v \in \mathbb{R}^{T \times D}$. In the case of MEMP, where gaze data is not available, we only fuse the scene vectors.

Time-Series Forecasting. Next, we merge (along the feature dimension) the motion features $m_{1:T}$ and the aforementioned fused features $v_{1:T}$ to obtain $[m_{1:T}, v_{1:T}] \in \mathbb{R}^{T \times 2 \cdot D}$. This forms the input for our time-series forecasting component \mathcal{T} , which takes the merged features $[m_{1:T}, v_{1:T}]$

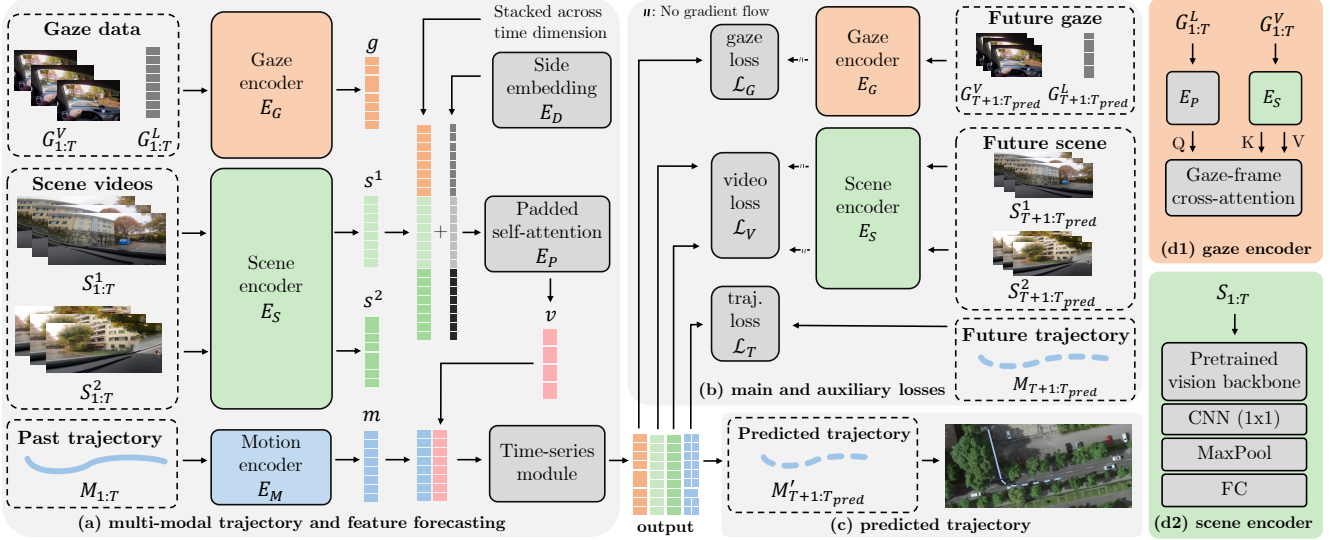


Figure 6. **Our G-MEMP framework.** The multimodal architecture fuses gaze, scene, and motion data for ego-trajectory forecasting (a). The scene videos are encoded with the scene encoder E_S frame-wise using a pre-trained vision backbone (d1). Video from the driver view in the gaze data is also encoded with the same E_S , and passed through a gaze-frame cross-attention (d2). The resulting tensors, all in the image feature domain, are stacked across time, self-attended, and concatenated with motion features for forecasting. G-MEMP predicts the trajectory (c), as well as features from gaze and video modalities concurrently to use them as auxiliary losses for regularization (b).

and produces a prediction of the future motion $M_{T:T_{\text{pred}}}$. For this task, we experiment with the state-of-the-art long-term time-series prediction methods Informer [55], Transformer [47], PatchTST [27] and NLinear/DLinear [51]. While the focus is on future trajectory prediction, we also predict future scene features $s_{T:T_{\text{pred}}}^{1:K}$ and, in the case of G-MEMP, future gaze features $g_{T:T_{\text{pred}}}$. The auxiliary outputs are essential for regularization during training by enforcing intermediate features to remain rich in scene- and gaze-related information, whenever available.

5.3. Training Objectives

Trajectory prediction models are prone to overfitting due to the inherent difficulty of the training regime: as the subsequent predictions depend on the correctness of the previous forecasts, models might learn from spurious correlations of the later sections of the trajectory. To tackle this problem, G-MEMP employs a novel loss formulation which we term as “future-discounted loss”. The principle behind this loss is to consider predictions for future time steps with diminishing weight, particularly at the early stages of the training, making predictions for the immediate future more influential on the overall loss than those for the distant future. This also follows real-world use cases where immediate predictions often have a higher impact than long-term predictions.

Future-discounted loss. Given a predicted sequence \mathbf{y}_{pred} and a ground truth sequence \mathbf{y}_{gt} , the future-discounted loss

\mathcal{L}_{fd} over N time steps is then defined as:

$$\mathcal{L}_{\text{fd}}(\mathbf{y}_{\text{pred}}, \mathbf{y}_{\text{gt}}) = \sum_{i=1}^N \gamma^i (\mathbf{y}_{\text{pred},i} - \mathbf{y}_{\text{gt},i})^2$$

where γ is the discount factor with $0 < \gamma < 1$. For adaptive learning, γ is initialized with a small value (e.g., 0.9) in the early epochs and is gradually increased (e.g., up to 0.99), challenging the model as it learns to predict the near future.

Loss composition. Both the primary trajectory loss and the auxiliary losses are subject to the future-discounted principle. Let \mathcal{L}_T denote the discounted trajectory loss, \mathcal{L}_V the discounted video loss and \mathcal{L}_G the discounted gaze loss. See Sup. Mat. for detailed definitions. The combined loss $\mathcal{L}_{\text{combined}}$ can be expressed as:

$$\mathcal{L}_{\text{combined}} = \mathcal{L}_T + \alpha_V \mathcal{L}_V + \alpha_G \mathcal{L}_G.$$

The coefficients α_V and α_G dynamically balance the primary and auxiliary losses. They are determined by:

$$\alpha_{V|G} = \rho_{V|G} \times \frac{\|\mathcal{L}_T\|}{\|\mathcal{L}_{V|G}\|}.$$

Here, $\rho_{V|G}$ is a scalar hyperparameter, and operator $\|\cdot\|$ represents the scalar value of a given parameter, detached from the gradient computation graph. This formulation ensures that auxiliary losses’ contribution to $\mathcal{L}_{\text{combined}}$ remains consistently proportional to \mathcal{L}_T , allowing for stabilized influence even if the auxiliary losses vary during training. Through this combined loss, the primary objective of trajectory prediction remains at the forefront, while the auxiliary losses aid in model regularization and training stability.

5.4. Implementation Details

G-MEMP is trained using the AdamW optimizer with a linear warm-up of 25 epochs and cosine annealing, over a total of 250 epochs. Maximum learning rate of 5×10^{-4} and weight decay of 0.05 are used with batch size 16. A full set of hyperparameters can be found in Sup. Mat.

Regularization. Dropout is extensively employed. We observe that both attention dropouts, and aggressive within-modality dropouts (e.g., dropping one of the two scene videos) both improve validation scores.

Caching. To benefit from pre-trained vision backbones while keeping the training duration under control, we have implemented module-level caching that utilizes intermediate features extracted from these backbones. Details of the caching mechanism are explained in Sup. Mat.

6. Experiments

We evaluate our method G-MEMP by measuring the predicted motion trajectories using a set of standard metrics. We compare against several state-of-the-art methods and baselines. Please see the Sup. Mat. for more results and examples.

6.1. Setup

Datasets. We evaluate our method on our proposed GEM dataset. To demonstrate that the benefit from gaze extends beyond our dataset, we additionally train and evaluate our framework on a second dataset. **Dr(eye)ve** [31] has 6 hours of driving along with gaze input, and contains scenes from rural, urban, and highway driving. Although it provides a similar setting to GEM, overall data quality including the gaze and GPS positions is significantly lower, with lower gaze frequency, and only a single scene camera.

Task. Following the task setting in nuScenes [5], our task uses 8-second input trajectories to predict the next 6-second motion. We sample synchronized sequences of location, videos, and gaze data with a sliding window of 2-second strides. To avoid overly simple trajectories, we only take segments of predetermined minimum PCI values. For our 8s/6s split, we determine that $PCI \geq 20$ is sufficient, resulting in approximately 4 hours for the training split.

Baselines. We use two simple baselines. **Stationary** baseline assumes that the vehicle remains stationary throughout the prediction window. **Linear** baseline assumes that the vehicle maintains a linear trajectory, following the vehicle’s final direction and speed from the input.

Motion prediction models. We compare our model with two gaze-assisted human motion prediction models adapted from the literature. **Multimodal Transformer** [21] encodes the input modalities with linear layers and predicts the future trajectory with an encoder/decoder architecture. In addition, We adapt **GIMO** [54] to utilize scene videos instead

Method	GEM		Dr(eye)ve	
	ADE (m)	FDE (m)	ADE (m)	FDE (m)
Stationary Baseline	26.33	164.79	61.41	385.17
Linear Baseline	15.18	103.36	15.54	107.34
Multimodal Transformer [21]	12.60	82.88	19.12	126.60
GIMO [54]	12.47	81.73	18.64	125.35
Ours - MEMP (video)	10.38	68.81	15.31	103.83
Ours - G-MEMP (video+gaze)	9.99	66.29	14.43	98.06

Table 2. **Comparison to baselines and SOTA.** We use the test sets of both the proposed dataset and the Dr(eye)ve dataset for evaluation. Our model G-MEMP achieves the best performance on both datasets.

of 3D point clouds and predict the future trajectory with a cross-modal encoder architecture.

Metrics. We use the standard evaluation metrics Average Displacement Error (ADE) and Final Displacement Error (FDE). **ADE** measures the average error between the ground truth and predicted trajectory across all time steps. **FDE** measures the displacement error at the final prediction time step, emphasizing the model’s accuracy in predicting the endpoint of a trajectory.

6.2. Evaluation of G-MEMP

Comparison to baselines and SOTA. We report results on the test sets of both our proposed dataset GEM and the Dr(eye)ve dataset in Table 2. Our model G-MEMP outperforms all baselines across both evaluation metrics and, therefore achieving state-of-the-art performance on both datasets.

Evaluating the benefit of utilizing gaze. We compare G-MEMP with MEMP - its version that does not make use of gaze information, in Table 2. We observe that the use of the gaze modality in G-MEMP is responsible for a significant improvement in the performance. This shows that gaze information holds an important role in the task of ego-trajectory prediction.

Qualitative evaluation. For sample qualitative results, see Figure 7 and Sup. Mat.

Evaluation across path complexity. As linear trajectories are trivial to model, we expect gaze to be most useful as a cue in complex and possibly ambiguous trajectories - cross-road turns, road bends, and non-linear segments. Therefore, using our established PCI metric, we divide our test data into groups - each representing a different level of path complexity. We evaluate and compare both G-MEMP and MEMP on each of the groups on Figure 8. It can be observed that as the target trajectory becomes more irregular, using gaze indeed offers an increasingly sizeable improvement over the task, with **4.76m** (20%) improvement in ADE in the 76+ PCI range.

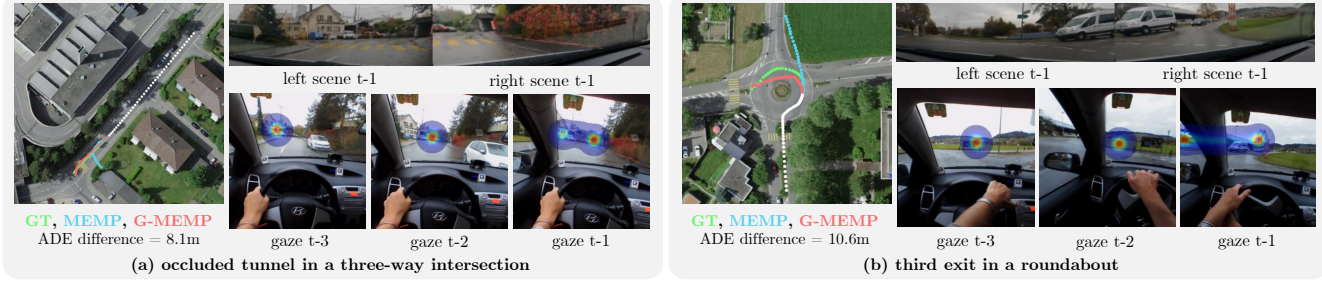


Figure 7. **Two examples where gaze provides an advantage.** In example (a), a three-way intersection splits into two just before a tunnel on the right. The scene model cannot act upon this rare structure and attempts to turn left, while the gaze model forecasts correctly. In example (b), the scene model observes an empty road ahead and tries to exit the roundabout, while the gaze model figures out the correct exit.

Method	Val. ADE (m)	Val. FDE (m)
Vanilla G-MEMP	8.85	58.54
+ auxiliary losses	8.68 (-0.17)	57.09 (-1.45)
+ future-discounted loss	8.27 (-0.41)	54.38 (-2.71)

Table 3. **Loss ablations.** GEM validation set is used.

6.3. Ablation Studies

We performed a series of ablation studies to determine the appropriate vision backbones and time series modules for our framework, as well as to justify the use of discounted and auxiliary losses.

Auxiliary and discounted losses. As one of the major contributions of our framework, we assess the contribution of the future-discounted loss \mathcal{L}_{fd} and the auxiliary losses through other modalities. Both additions show significant improvement over the standard architecture on the validation set, as seen in Table 3.

Time-series module. Informer [55] is a Transformer-based model and leverages the ProbSparse attention mechanism.

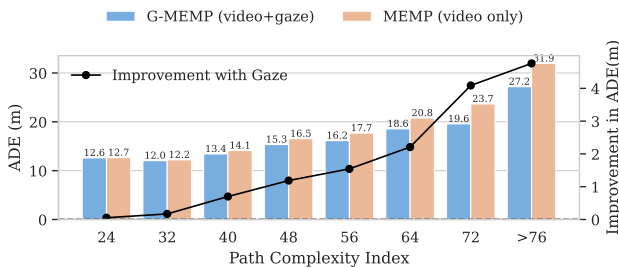


Figure 8. **The effect of using gaze over different PCI.** Lower is better for ADE, and higher is better for ADE Improvement. The test set of Dr(eye)ve was divided into groups based on the Path Complexity Index. The bars show the average ADE of each model in each of the groups centered at the shown PCI value. The line corresponds to the difference between the ADE of MEMP and G-MEMP- higher means more difference in favor of G-MEMP.

Method	Val. ADE (m)	Val. FDE (m)
DLinear [51]	10.67	81.40
NLinear [51]	10.49	83.38
PatchTST [27]	10.23	79.80
Transformer [47]	9.97	67.88
Informer [55]	9.62	66.14
Informer+SAM [20]	9.08	57.89
Informer+DinoV2 [29]	8.69	60.83
Informer+SwinV2 [22]	8.51	55.56

Table 4. **Visual encoder and time-series module ablations.** GEM validation set is used. Time-series modules (top) perform prediction with motion as input, without scene or gaze data. Pre-trained vision modules (bottom) use Informer as the time-series module.

Table 4 shows that Informer consistently outperforms later models such as Autoformer [49], LTSF-Linear [51], and PatchTST [27]. We used Informer in G-MEMP.

Pretrained vision backbone. In Table 4, we evaluate the impact of various visual encoders including SAM (Segment Anything) [20], DinoV2 [29] and SwinV2 [22]. SwinV2 consistently demonstrated superior performance on the validation set with smaller embedding sizes than its counterparts and is exclusively used in G-MEMP.

7. Conclusion

Our findings underscore the value of utilizing gaze as a source of intent information for ego-vehicle trajectory prediction. This is efficiently done with our novel multimodal approach G-MEMP, combining gaze, scene, and motion data. It achieves superior results to the established baselines and advances state-of-the-art performance on the task. Specifically, we find that utilizing gaze allows for better forecasting of complex non-linear trajectories. Confirming the significant potential of gaze for driving, we set a benchmark in the field with our proposed GEM dataset, paving the way for more intuitive and human-centric advancements in assisted driving technologies.

G-MEMP: Gaze-Enhanced Multimodal Ego-Motion Prediction in Driving

Supplementary Material

A. GEM Dataset

A.1. Breakdown of GEM Dataset and PCI Insights

For the information on the dataset split and the behavior of each participant, see [Table 5](#).

A deeper dive into our dataset, combined with synchronization with OpenStreetMap [28], reveals that the high PCI events indeed happen either close to the intersections, or on trajectories with a high-speed change, as observed in [Figure 9](#).

B. Ground Truth Correction with GPSLABELER

GPS data, particularly those collected using devices like GoPro cameras, can often be noisy and potentially inaccurate due to various reasons, ranging from satellite interference to obstructions like tall buildings or tunnels. Such inaccuracies in geospatial data can severely hamper the reliability and utility of a dataset, especially when the data is intended for detailed analysis and modeling. Examples of such cases, as well as milder issues, can be seen in [Figure 10](#).

In response to this challenge, we have developed the desktop tool GPSLABELER, designed to facilitate the correction of noisy GPS data. The primary strength of GPSLABELER lies in its unique user interface which juxtaposes the video feed and the associated GPS location points on a map. This side-by-side presentation enables users to

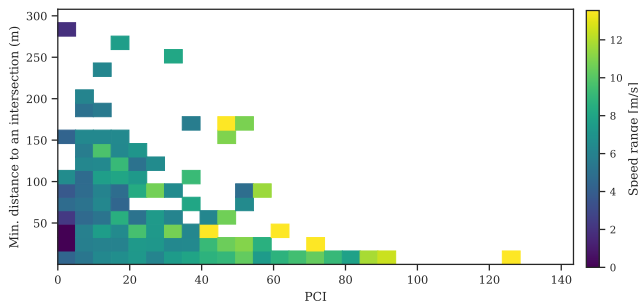


Figure 9. **Function of PCI with respect to the distance to an intersection.** Speed range—the difference between the highest and lowest instantaneous speed throughout the trajectory—is chosen instead of speed as high yet constant speed without a change in direction (e.g. cruising on a highway) is a low-PCI event. Bins with multiple samples are displayed, with a median speed range per bin. PCI is highly correlated with distance to an intersection, but only if a vehicle changes its speed throughout the trajectory, which discards stoppings and straight driving cases.

cross-verify the video content with the GPS coordinates visually.

Using the application is intuitive and straightforward, an example of which can be seen in Figure 3 in the main paper. As users watch the video playback, they can simultaneously observe the GPS path on the map. If discrepancies are noted, users can manually re-label the GPS data by simply clicking on the map and dragging the points to the desired accurate location. One key feature of GPSLABELER is its interpolation mechanism. Once users adjust certain key points on the map, the application automatically interpolates the GPS data between these points, ensuring smooth and consistent transitions.

Designed with user-friendliness in mind, GPSLABELER is cross-platform, with versions available for Windows, MacOS, and Linux. This ensures that researchers and dataset curators across diverse technological environments can access and utilize the tool to enhance the accuracy of their geospatial data.

C. Dataset Postprocessing

C.1. Gaze Fixation Detection

For our fixation detection, we adopted the methodology from Pupil Labs, the creators of the glasses embedded with gaze detectors [43]. Our criteria define gaze fixations as instances where the gaze remains relatively stationary for a duration ranging from 80ms to 1 second. The upper limit of this range, 1 second, could also characterize a smooth pursuit, where the eyes smoothly track a moving object. Furthermore, we account for dispersion, which represents the spatial movement permitted within a single fixation. A gaze group is considered a fixation if the dispersion is within a limit of 1.5 degrees, ensuring that minor involuntary or random gaze movements do not undermine the detection of

Subject	Total Distance (m)	Rainy	PCI (mean)	PCI (max)	Split
001	13,112	✓	12.37	92.99	train
002	12,824	✓	10.76	81.22	val.
003	12,997	✗	20.09	94.87	train
004	13,064	✗	14.59	79.30	val.
005	12,872	✗	17.29	86.39	train
006	13,127	✗	13.82	88.00	train
007	12,973	✗	16.42	77.47	train
008	13,700	✓	17.02	89.48	test
009	12,958	✗	15.30	103.96	test
010	13,048	✗	14.63	81.42	train

Table 5. **Breakdown of our GEM dataset.** We report duration, weather condition, and PCI for each participant.

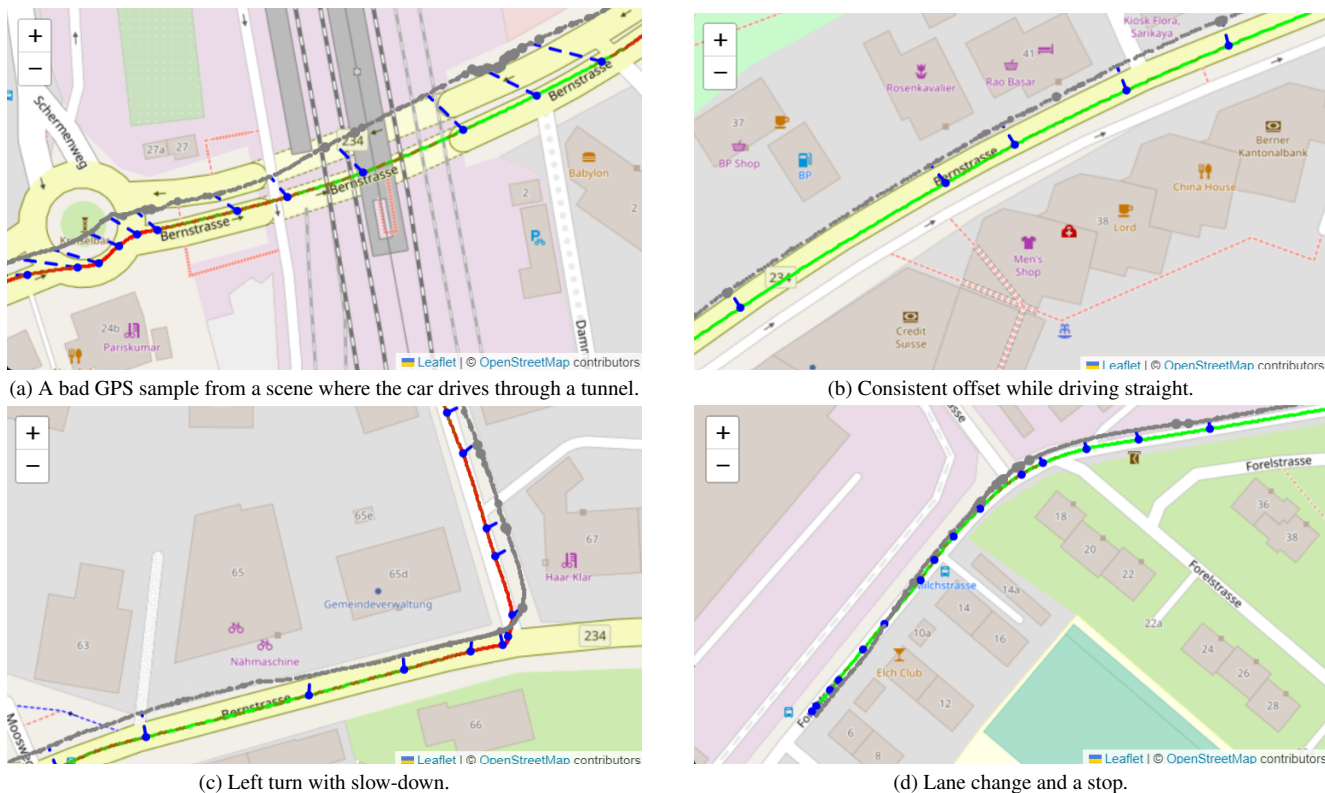


Figure 10. **Example trajectory fixes with GPSTABLER**. The original GPS points are in gray, and the hand-placed markers are blue. The new markers are interpolated with a cubic spline with a color that represents the instantaneous speed: red for slow, and green for fast movement.

genuine fixations.

A set of example fixations can be seen in Figure 12. Note that there are frames without any detected fixations, which is explained by saccades and blinks. For others, the accuracy is high: note how the gaze meets exactly with the brake light of the bus in front, in Scene 1, Frame 9. Similarly, the gaze over the motorcycle in front is well-centered in Scene 5 for most frames.

C.2. Exploring Image Homography and Stitching

In our dataset, we provide synchronized videos from different viewpoints. In an attempt to provide a fully registered view from multiple cameras to our model, we have explored approaches for stitching them. However, we have discovered that using the separate videos brings benefits:

- Using the current state of the art, it is not feasible to register the driver head-cam frames and the scene videos within an acceptable error margin. We experimented with classical feature extractors such as DISK [44], as well as transformer-based detector-free local feature matching [41], using Kornia library [33].
- We have observed that the redundancy from having multiple scene camera feeds can be exploited for training regu-

larization. By dropping out one of the views at each frame during training, we were able to improve the validation performance.

Example frames from the stitching experiments can be seen in Figure 11.



Figure 11. **Successful and failed stitching examples**. We used LoFTR for feature-matching across scene videos and the head-cam.

D. G-MEMP

Using the notation we have established, our full model can be described as:

$$\Psi(M_{1:T}, S_{1:T}^{1:K}, G_{1:T}|\lambda) \equiv \mathcal{T}(E_M(M_{1:T}), E_P(E_S(S_{1:T}^{1:K})), E_G(G_{1:T})) = \{M'_{T:T_{\text{pred}}}, s_{T:T_{\text{pred}}}^{1:K}, g_{T:T_{\text{pred}}}\}$$

Loss definitions. For the model outputs $\Psi(M_{1:T}, S_{1:T}^{1:K}, G_{1:T}|\lambda) = \{M'_{T:T_{\text{pred}}}, s_{T:T_{\text{pred}}}^{1:K}, g_{T:T_{\text{pred}}}\}$, let \mathcal{L}_T denote the discounted trajectory loss, \mathcal{L}_V the discounted video loss and \mathcal{L}_G the discounted gaze loss. The auxiliary losses are defined as:

$$\begin{aligned} \mathcal{L}_T &= \mathcal{L}_{\text{fd}}(M'_{T:T_{\text{pred}}}, M_{T:T_{\text{pred}}}) \\ \mathcal{L}_V &= \sum_{i=1}^K \mathcal{L}_{\text{fd}}(s_{T:T_{\text{pred}}}^i, E_S(s_{T:T_{\text{pred}}}^i)) \\ \mathcal{L}_G &= \mathcal{L}_{\text{fd}}(g_{T:T_{\text{pred}}}, E_G(g_{T:T_{\text{pred}}})) \end{aligned}$$

D.1. Implementation Details

All experiments are carried out on a machine with an NVIDIA GPU with > 10 GB memory, 64 GB of RAM, and an Intel CPU. The framework is implemented using PyTorch 2.0.

D.2. Module-level Caching with MODULECACHE

Caching is a crucial component of our training regime. During the initial epochs, the intermediate representations from the pre-trained vision backbones are computed for each input frame and stored in an efficient cache memory structure. When subsequent epochs require the same input data, the pre-computed representations are fetched from the cache, thereby eliminating the need for repetitive and costly forward passes through the vision backbones.

To make this process repeatable, we implemented the MODULECACHE utility to provide a generic caching mechanism. The MODULECACHE library offers an easy way to cache the outputs of PyTorch modules, making it particularly suited for our need to efficiently cache the outputs of large, pre-trained vision transformers.

D.2.1 Key Features

The MODULECACHE library offers several notable features:

- Allows caching of PyTorch module outputs in two formats: in-memory for fast retrieval, and persistently on the disk for larger datasets.
- Adopts a decorator-based interface that simplifies its integration with PyTorch modules.

- Implements an MRU (most-recently-used) cache policy to manage and limit memory or disk consumption.

D.2.2 Usage

The library’s decorator-based design ensures minimal modifications to the existing PyTorch codebase. By adding the `@modulecache()` decorator, the output of the module’s forward method gets cached, as illustrated in the provided basic usage example:

```

1 from @
2 class MyModule(nn.Module):
3     def init(self):
4         super().init()
5         self.linear = nn.Linear(10, 10)
6     def forward(self, x):
7         # This output will be cached
8         return self.linear(x)

```

More detailed examples, advanced usage patterns, and further documentation will be accessible at the official MODULECACHE documentation.

D.2.3 Operational Assumptions

For the MODULECACHE library to operate seamlessly, there are certain assumptions that the PyTorch modules should adhere to:

1. The module should be a subclass of `nn.Module`.
2. The forward method of the module should be capable of accepting any number of positional arguments with shapes denoted by $(B, *)$, where B stands for the batch size, and $*$ denotes any other dimensions.
3. All input tensors should be located on the same computational device and should share the same data type (dtype).
4. The method should return a single tensor with the shape $(B, *)$.

The MODULECACHE library has proven invaluable in our experiments by allowing us to efficiently utilize the outputs of our pre-trained vision transformers without incurring significant computational overhead.

E. Experiments

E.1. Evaluation Metrics

The Average Displacement Error (ADE) is formally defined as:

$$\text{ADE} = \frac{1}{T} \sum_{t=1}^T \|\mathbf{p}_t^{\text{pred}} - \mathbf{p}_t^{\text{gt}}\|_2, \quad (1)$$

where T is the total number of prediction time steps, $\mathbf{p}_t^{\text{pred}}$ is the predicted position at time t , and \mathbf{p}_t^{gt} is the ground truth position at the same time.

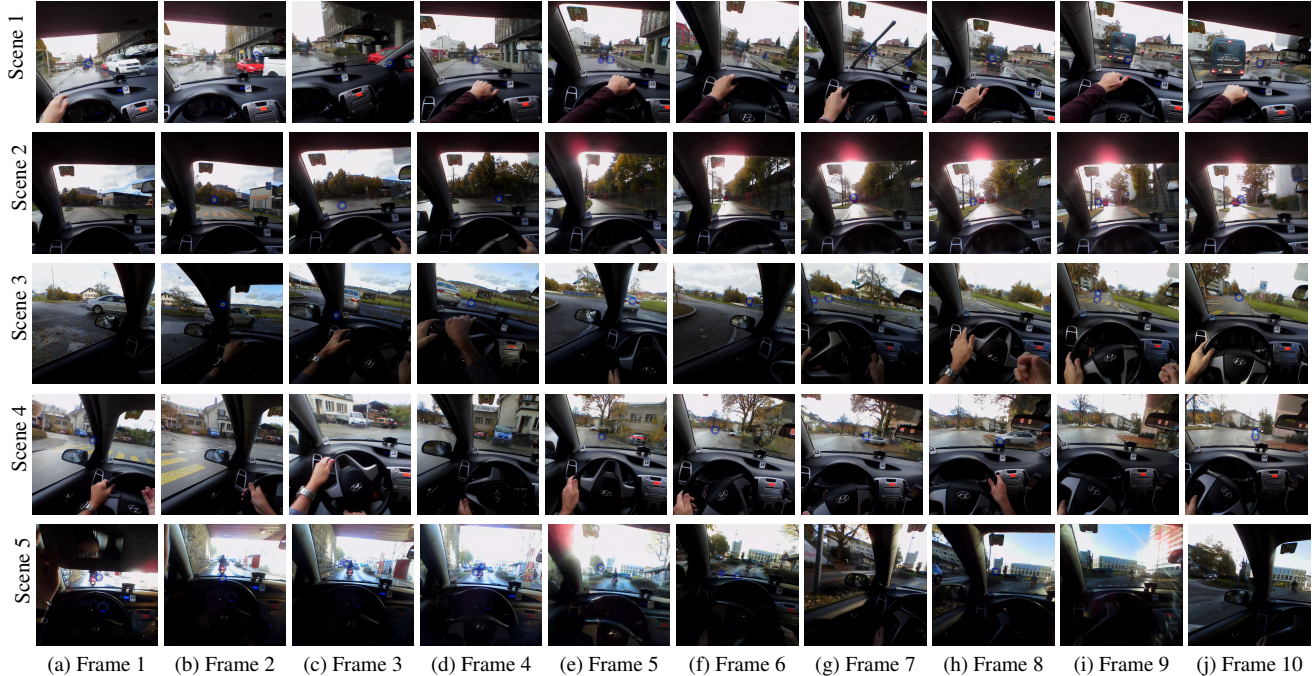


Figure 12. **Visual representation of gaze heatmaps across different scenes in the dataset.** Each scene row is visualized with a sample of 10 frames with a one-second time difference, illustrating gaze patterns over time. Note that fixations are not always available due to blinks and saccades.

Table 6. Training configurations

Parameter	Value
Optimizer	AdamW
Learning rate	0.0005
Weight decay	0.05
Epochs	250
Epsilon	1
Scene video FPS	1
Gaze video FPS	1
Batch size	4
Output FPS	5
Min PCI	20
Loss discount factor/epoch	[0: 0.9, 100: 0.95, 200: 0.99]

The Final Displacement Error (FDE) is the displacement error at the final prediction time step:

$$\text{FDE} = \|\mathbf{p}_T^{\text{pred}} - \mathbf{p}_T^{\text{gt}}\|_2. \quad (2)$$

E.2. Hyperparameters

The hyperparameters for the experiments can be found in [Table 6](#), [Table 7](#), [Table 8](#), and [Table 9](#).

Table 7. Framework configurations

Parameter	Value
Encoder heads	8
Encoder layers	3
Feature dropout	0.1
Dense prediction	true
Use angle and norm	true
Encoder hidden size	64
Gaze encoder layers	3
Gaze dropout	0.5
View dropout	1
Maxpool kernel size	8
Front video scaling factor	0.3
Scene video scaling factor	0.1
Gaze decoder dropout	0.1
Image embedding size	64
Dense gaze loss ratio	0.2
Dense video loss ratio	0.2
Normalize video features	true

E.3. Qualitative analysis of MEMP

We have shown that by utilizing gaze, G-MEMP is able to make better predictions in certain (high path complexity) situations, as explored in [Figure 7](#). While driver intention

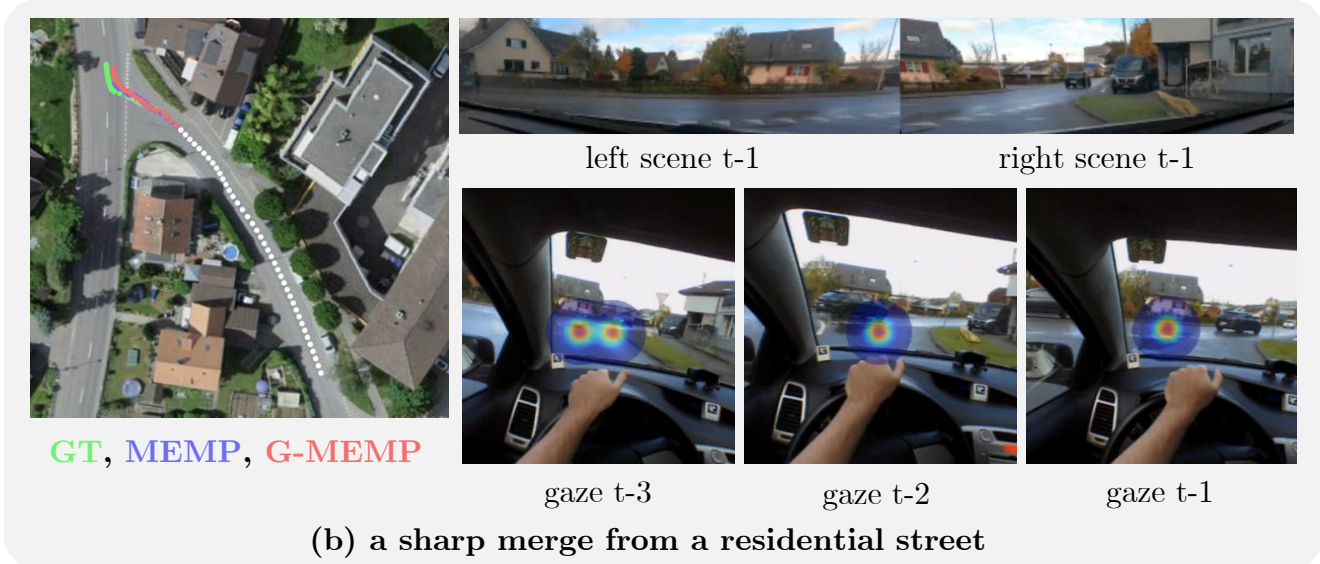
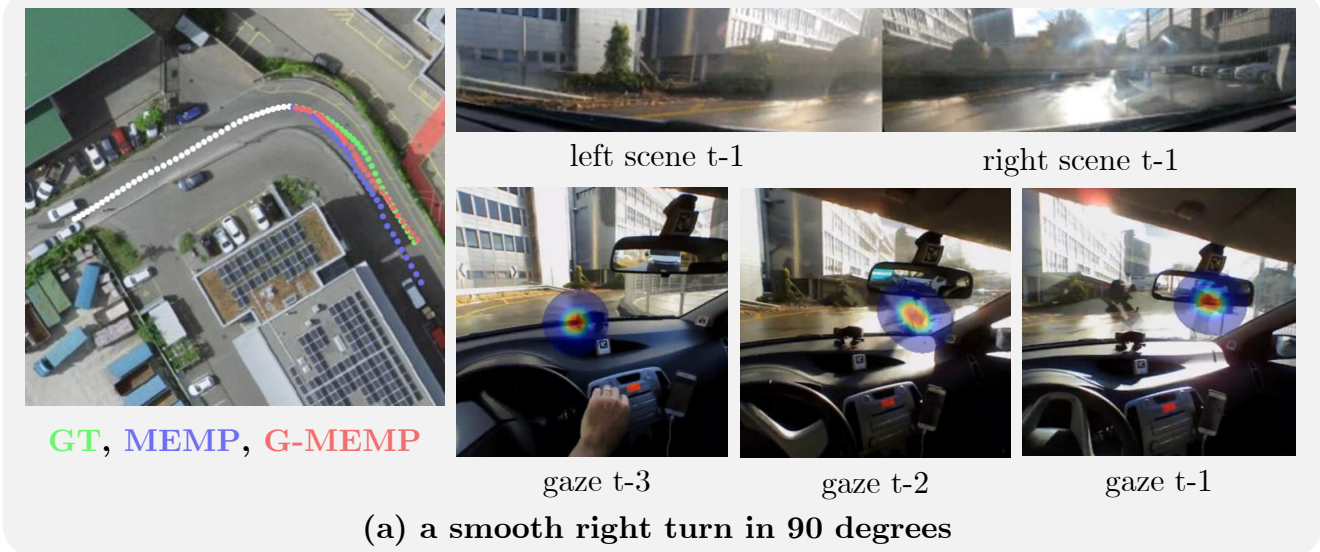


Figure 13. **Two simple intersections where both gaze and video models are successful.** In example (a), there is a 90-degree right turn with the correct curvature estimated by both the gaze and video models. G-MEMP is better at predicting the speed for the later stages of the trajectory. In example (b), both models have a near-identical prediction for a sharp merge from a residential road to a main street.

prediction is important in these cases, we notice that for many simpler straightforward cases, predictions based on scene and trajectory information are already quite accurate. In [Figure 13](#), we demonstrate the performance of MEMP. In these examples, there is an obvious turn that the driver can make, and the curvature of the trajectory is determined by the roads in front, which MEMP model is successful in figuring out without extra driver information.

Table 8. GPS backbone (Informer) configurations

Parameter	Value
Distil	true
Factor	1
Model dimension	128
Dropout	0.1
Number of Heads	8
Sequence Length	40
Decoder layers	2
Encoder layers	3
Prediction Length	30
Label Length	40
With Gaze	true
Activation	gelu
Individual	false
Moving average	25

Table 9. Video backbone (SwinV2) configuration

Parameter	Value
Model Type	swinv2_base_window12to16_192to256
Pad to square	true
Train backbone	false

References

- [1] Roland Allenbach, Steffen Niemann, Yvonne A. Stürmer, Patrizia Hertach, Karin Huwiler, and Jasmin Zimmermann. Sinus 2021 – sicherheitsniveau und unfallgeschehen im strassenverkehr 2020. Bern: BFU, Beratungsstelle für Unfallverhütung, 2021. 1
- [2] Samer Ammoun and Fawzi Nashashibi. Real time trajectory prediction for collision risk estimation between vehicles. In *2009 IEEE 5Th international conference on intelligent computer communication and processing*, pages 417–422. IEEE, 2009. 2
- [3] Michael Argyle, Mark Cook, and Duncan Cramer. Gaze and mutual gaze. *The British Journal of Psychiatry*, 165(6): 848–850, 1994. 1, 2
- [4] Ulrich Baumann, Claudius Guiser, Michael Herman, and J Marius Zollner. Predicting ego-vehicle paths from environmental observations with a deep neural network. In *2018 IEEE International Conference on Robotics and Automation (ICRA)*, pages 4709–4716. IEEE, 2018. 2
- [5] Holger Caesar, Varun Bankiti, Alex H. Lang, Sourabh Vora, Venice Erin Liong, Qiang Xu, Anush Krishnan, Yu Pan, Giancarlo Baldan, and Oscar Beijbom. nuscenes: A multi-modal dataset for autonomous driving. In *CVPR*, 2020. 3, 7
- [6] Thomas Eiter and Heikki Mannila. Computing discrete fréchet distance. 1994. 4
- [7] Scott Ettinger, Shuyang Cheng, Benjamin Caine, Chenxi Liu, Hang Zhao, Sabeek Pradhan, Yuning Chai, Benjamin Sapp, Charles R. Qi, Yin Zhou, Zoey Yang, Aurelien Chouard, Pei Sun, Jiquan Ngiam, Vijay Vasudevan, Alexander McCauley, Jonathon Shlens, and Dragomir Anguelov. Large scale interactive motion forecasting for autonomous driving : The waymo open motion dataset. *CoRR*, abs/2104.10133, 2021. 3
- [8] Xidong Feng, Zhepeng Cen, Jianming Hu, and Yi Zhang. Vehicle trajectory prediction using intention-based conditional variational autoencoder. In *2019 IEEE Intelligent Transportation Systems Conference (ITSC)*, pages 3514–3519. IEEE, 2019. 2
- [9] F. N. Fritsch and J. Butland. A method for constructing local monotone piecewise cubic interpolants. *SIAM Journal on Scientific and Statistical Computing*, 5(2):300–304, 1984. 4
- [10] Shreya Ghosh, Abhinav Dhall, Garima Sharma, Sarthak Gupta, and Nicu Sebe. Speak2label: Using domain knowledge for creating a large scale driver gaze zone estimation dataset. In *Proceedings of the IEEE/CVF International Conference on Computer Vision*, pages 2896–2905, 2021. 2
- [11] Harshayu Girase, Haiming Gang, Srikanth Malla, Jiachen Li, Akira Kanehara, Karttikeya Mangalam, and Chiho Choi. Loki: Long term and key intentions for trajectory prediction. In *Proceedings of the IEEE/CVF International Conference on Computer Vision*, pages 9803–9812, 2021. 3, 4
- [12] Klokan Technologies GmbH. Wgs 84 / pseudo-mercator - spherical mercator. 5
- [13] Junru Gu, Chen Sun, and Hang Zhao. Densettnt: End-to-end trajectory prediction from dense goal sets. In *Proceedings of the IEEE/CVF International Conference on Computer Vision (ICCV)*, pages 15303–15312, 2021. 1, 2
- [14] Mahir Gulzar, Yar Muhammad, and Naveed Muhammad. A survey on motion prediction of pedestrians and vehicles for autonomous driving. *IEEE Access*, 9:137957–137969, 2021. 2
- [15] Mary M. Hayhoe, Anurag Shrivastava, Ryan Mruzek, and Jeff B. Pelz. Visual memory and motor planning in a natural task. *Journal of Vision*, 3(1):6–6, 2003. 1, 2
- [16] Yanjun Huang, Jiatong Du, Ziru Yang, Zewei Zhou, Lin Zhang, and Hong Chen. A survey on trajectory-prediction methods for autonomous driving. *IEEE Transactions on Intelligent Vehicles*, 7(3):652–674, 2022. 2
- [17] Ashesh Jain, Hema S. Koppula, Bharad Raghavan, Shane Soh, and Ashutosh Saxena. Car that Knows Before You Do: Anticipating Maneuvers via Learning Temporal Driving Models. In *2015 IEEE International Conference on Computer Vision (ICCV)*, pages 3182–3190, Santiago, Chile, 2015. IEEE. 2
- [18] ByeoungDo Kim, Chang Mook Kang, Jaekyum Kim, Seung Hi Lee, Chung Choo Chung, and Jun Won Choi. Probabilistic vehicle trajectory prediction over occupancy grid map via recurrent neural network. In *2017 IEEE 20Th international conference on intelligent transportation systems (ITSC)*, pages 399–404. IEEE, 2017. 2
- [19] Dongchan Kim, Hyukju Shon, Nahyun Kweon, Seungwon Choi, Chanuk Yang, and Kunsoo Huh. Driving style-based conditional variational autoencoder for prediction of ego vehicle trajectory. *IEEE Access*, 9:169348–169356, 2021. 2
- [20] Alexander Kirillov, Eric Mintun, Nikhila Ravi, Hanzi Mao, Chloe Rolland, Laura Gustafson, Tete Xiao, Spencer Whitehead, Alexander C. Berg, Wan-Yen Lo, Piotr Dollár, and Ross Girshick. Segment anything. *arXiv:2304.02643*, 2023. 5, 8
- [21] Ruilong Li, Shan Yang, David A. Ross, and Angjoo Kanazawa. Ai choreographer: Music conditioned 3d dance generation with aist++, 2021. 7
- [22] Ze Liu, Han Hu, Yutong Lin, Zhuliang Yao, Zhenda Xie, Yixuan Wei, Jia Ning, Yue Cao, Zheng Zhang, Li Dong, Furu Wei, and Baining Guo. Swin transformer V2: scaling up capacity and resolution. *CoRR*, abs/2111.09883, 2021. 5, 8
- [23] Kedi Lyu, Haipeng Chen, Zhenguang Liu, Beiqi Zhang, and Ruili Wang. 3d human motion prediction: A survey. *Neurocomputing*, 489:345–365, 2022. 2
- [24] Srikanth Malla, Behzad Dariush, and Chiho Choi. Titan: Future forecast using action priors. In *Proceedings of the IEEE/CVF Conference on Computer Vision and Pattern Recognition*, pages 11186–11196, 2020. 2
- [25] Nigamaa Nayakanti, Rami Al-Rfou, Aurick Zhou, Kratarth Goel, Khaled S Refaat, and Benjamin Sapp. Wayformer: Motion forecasting via simple & efficient attention networks. In *2023 IEEE International Conference on Robotics and Automation (ICRA)*, pages 2980–2987. IEEE, 2023. 1, 2
- [26] Jiquan Ngiam, Benjamin Caine, Vijay Vasudevan, Zhengdong Zhang, Hao-Tien Lewis Chiang, Jeffrey Ling, Rebecca Roelofs, Alex Bewley, Chenxi Liu, Ashish Venugopal, et al. Scene transformer: A unified architecture for predicting mul-

- tiple agent trajectories. *arXiv preprint arXiv:2106.08417*, 2021. 1, 2
- [27] Yuqi Nie, Nam H. Nguyen, Phanwadee Sinthong, and Jayant Kalagnanam. A time series is worth 64 words: Long-term forecasting with transformers. In *International Conference on Learning Representations*, 2023. 6, 8
- [28] OpenStreetMap contributors. Planet dump retrieved from <https://planet.osm.org>. <https://www.openstreetmap.org>, 2017. 9
- [29] Maxime Oquab, Timothée Darcet, Theo Moutakanni, Huy V. Vo, Marc Szafraniec, Vasil Khalidov, Pierre Fernandez, Daniel Haziza, Francisco Massa, Alaaeldin El-Noby, Russell Howes, Po-Yao Huang, Hu Xu, Vasu Sharma, Shang-Wen Li, Wojciech Galuba, Mike Rabbat, Mido Assran, Nicolas Ballas, Gabriel Synnaeve, Ishan Misra, Herve Jegou, Julien Mairal, Patrick Labatut, Armand Joulin, and Piotr Bojanowski. Dinov2: Learning robust visual features without supervision, 2023. 5, 8
- [30] Juan Diego Ortega, Neslihan Kose, Paola Cañas, Min-An Chao, Alexander Unnervik, Marcos Nieto, Oihana Otaegui, and Luis Salgado. Dmd: A large-scale multi-modal driver monitoring dataset for attention and alertness analysis. In *Computer Vision—ECCV 2020 Workshops: Glasgow, UK, August 23–28, 2020, Proceedings, Part IV 16*, pages 387–405. Springer, 2020. 2
- [31] Andrea Palazzi, Davide Abati, Simone Calderara, Francesco Solera, and Rita Cucchiara. Predicting the driver’s focus of attention: the dr(eye)ve project. *IEEE Transactions on Pattern Analysis and Machine Intelligence*, 2018. 2, 3, 4, 7
- [32] Hyun Soo Park, Jyh-Jing Hwang, Yedong Niu, and Jianbo Shi. Egocentric future localization. In *Proceedings of the IEEE Conference on Computer Vision and Pattern Recognition*, pages 4697–4705, 2016. 2
- [33] Edgar Riba, Dmytro Mishkin, Daniel Ponsa, Ethan Rublee, and Gary R. Bradski. Kornia: an open source differentiable computer vision library for pytorch. *CoRR*, abs/1910.02190, 2019. 10
- [34] Rafael F. Ribeiro and Paula D. P. Costa. Driver Gaze Zone Dataset With Depth Data. In *2019 14th IEEE International Conference on Automatic Face & Gesture Recognition (FG 2019)*, pages 1–5, 2019. 2
- [35] Ivan Rodin, Antonino Furnari, Dimitrios Mavroeidis, and Giovanni Maria Farinella. Predicting the future from first person (egocentric) vision: A survey. *Computer Vision and Image Understanding*, 211:103252, 2021. 2
- [36] Tim Salzmann, Boris Ivanovic, Punarjay Chakravarty, and Marco Pavone. Trajectron++: Dynamically-feasible trajectory forecasting with heterogeneous data. In *Computer Vision—ECCV 2020: 16th European Conference, Glasgow, UK, August 23–28, 2020, Proceedings, Part XVIII 16*, pages 683–700. Springer, 2020. 1, 2
- [37] Tim Salzmann, Boris Ivanovic, Punarjay Chakravarty, and Marco Pavone. Trajectron++: Dynamically-feasible trajectory forecasting with heterogeneous data, 2021. 5
- [38] Wilko Schwarting, Javier Alonso-Mora, and Daniela Rus. Planning and decision-making for autonomous vehicles. *Annual Review of Control, Robotics, and Autonomous Systems*, 1(1):187–210, 2018. 1, 2
- [39] Anke Schwarz, Monica Haurilet, Manuel Martinez, and Rainer Stiefelhagen. Drivehead—a large-scale driver head pose dataset. In *Proceedings of the IEEE Conference on Computer Vision and Pattern Recognition Workshops*, pages 1–10, 2017. 2
- [40] Krishna Kumar Singh, Kayvon Fatahalian, and Alexei A. Efros. KrishnaCam: Using a longitudinal, single-person, egocentric dataset for scene understanding tasks. In *2016 IEEE Winter Conference on Applications of Computer Vision (WACV)*, pages 1–9, Lake Placid, NY, USA, 2016. IEEE. 2
- [41] Jiaming Sun, Zehong Shen, Yuang Wang, Hujun Bao, and Xiaowei Zhou. LoFTR: Detector-free local feature matching with transformers. *CVPR*, 2021. 10
- [42] Izzeddin Teeti, Salman Khan, Ajmal Shahbaz, Andrew Bradley, and Fabio Cuzzolin. Vision-based intention and trajectory prediction in autonomous vehicles: A survey. In *Proceedings of the Thirty-First International Joint Conference on Artificial Intelligence, IJCAI-22*, pages 5630–5637. International Joint Conferences on Artificial Intelligence Organization, 2022. Survey Track. 4
- [43] Marc Tonsen, Chris Kay Baumann, and Kai Dierkes. A high-level description and performance evaluation of pupil invisible. *arXiv preprint arXiv:2009.00508*, 2020. 9
- [44] Michał J. Tyszkiewicz, Pascal Fua, and Eduard Trulls. Disk: Learning local features with policy gradient, 2020. 10
- [45] Geoffrey J Underwood, Peter Chapman, David Crundall, Sarah Cooper, and Robert Wallen. The visual control of steering and driving: Where do we look when negotiating curves? *Vision in vehicles*, 7:245–252, 1999. 2
- [46] Balakrishnan Varadarajan, Ahmed Hefny, Avikalp Srivastava, Khaled S Refaat, Nigamaa Nayakanti, Andre Cornman, Kan Chen, Bertrand Douillard, Chi Pang Lam, Dragomir Anguelov, et al. Multipath++: Efficient information fusion and trajectory aggregation for behavior prediction. In *2022 International Conference on Robotics and Automation (ICRA)*, pages 7814–7821. IEEE, 2022. 1, 2
- [47] Ashish Vaswani, Noam Shazeer, Niki Parmar, Jakob Uszkoreit, Llion Jones, Aidan N. Gomez, Lukasz Kaiser, and Illia Polosukhin. Attention is all you need, 2017. 6, 8
- [48] Benjamin Wilson, William Qi, Tanmay Agarwal, John Lambert, Jagjeet Singh, Siddhesh Khandelwal, Bowen Pan, Ratnesh Kumar, Andrew Hartnett, Jhony Kaesemodel Pontes, Deva Ramanan, Peter Carr, and James Hays. Argoverse 2: Next generation datasets for self-driving perception and forecasting. In *Proceedings of the Neural Information Processing Systems Track on Datasets and Benchmarks (NeurIPS Datasets and Benchmarks 2021)*, 2021. 3
- [49] Haixu Wu, Jiehui Xu, Jianmin Wang, and Mingsheng Long. Autoformer: Decomposition transformers with Auto-Correlation for long-term series forecasting. In *Advances in Neural Information Processing Systems*, 2021. 8
- [50] Zhanhong Yan, Bo Yang, Zheng Wang, and Kimihiko Nakano. A predictive model of a driver’s target trajectory based on estimated driving behaviors. *Sensors*, 23(3):1405, 2023. 2
- [51] Ailing Zeng, Muxi Chen, Lei Zhang, and Qiang Xu. Are transformers effective for time series forecasting? 2023. 6, 8

- [52] Weili Zeng, Xiao Chu, Zhengfeng Xu, Yan Liu, and Zhibin Quan. Aircraft 4d trajectory prediction in civil aviation: A review. *Aerospace*, 9(2):91, 2022. [2](#)
- [53] Mingfang Zhang, Yunfei Liu, and Feng Lu. GazeOnce: Real-Time Multi-Person Gaze Estimation. In *2022 IEEE/CVF Conference on Computer Vision and Pattern Recognition (CVPR)*, pages 4187–4196, New Orleans, LA, USA, 2022. IEEE. [1](#), [2](#)
- [54] Yang Zheng, Yanchao Yang, Kaichun Mo, Jiaman Li, Tao Yu, Yebin Liu, Karen Liu, and Leonidas Guibas. Gimo: Gaze-informed human motion prediction in context. In *ECCV*, 2022. [2](#), [7](#)
- [55] Haoyi Zhou, Shanghang Zhang, Jieqi Peng, Shuai Zhang, Jianxin Li, Hui Xiong, and Wancai Zhang. Informer: Beyond efficient transformer for long sequence time-series forecasting. In *The Thirty-Fifth AAAI Conference on Artificial Intelligence, AAAI 2021, Virtual Conference*, pages 11106–11115. AAAI Press, 2021. [5](#), [6](#), [8](#)